Reducing near-surface artifacts from the crossline direction by full-waveform inversion of interferometric surface waves

Liu, Jianhuan; Draganov, Deyan; Ghose, Ranajit

DOI
10.1190/geo2021-0613.1

Publication date
2022

Document Version
Final published version

Published in
Geophysics

GEOPHYSICS, VOL. 87, NO. 6 (NOVEMBER-DECEMBER 2022); P. R443–R452, 13 FIGS.
10.1190/GEO2021-0613.1

Reducing near-surface artifacts from the crossline direction by full-waveform inversion of interferometric surface waves

Jianhuan Liu[1], Deyan Draganov[1], and Ranajit Ghose[1]

ABSTRACT

Seismic incoherent noise and waves scattered from objects in the crossline directions can cause 2D elastic full-waveform inversion (FWI) to produce artifacts in the resulting 2D models. We develop a complete workflow that can determine subsurface S-wave velocity (V_S) models inverted from 2D near-surface seismic data more stably. We make use of a combination of supervirtual interferometry and a matched filter to accurately retrieve dominant surface waves from the field data, whereas the incoherent noise and 3D scattering events are significantly suppressed. The subsurface structures obtained from inverting the retrieved data can be interpreted together with the sections resulting from FWI of the original data to mitigate the potential misinterpretation of artifacts. Our results demonstrate that it is possible to invert 2D near-surface seismic data even when the data quality is lowered by the presence of strong noise and 3D scattered events caused by objects located in the crossline direction.

INTRODUCTION

Obtaining details of small-scale near-surface subsurface structures in a noninvasive way is an important issue in various fields of applications, such as geotechnical site investigation (Nguyen and Tran, 2018), groundwater management (Lambot et al., 2008), natural-hazard evaluation (Mecking et al., 2021), and archaeological prospecting (Dokter et al., 2017; Köhn et al., 2019). An appropriate method to resolve near-surface features is elastic full-waveform inversion (FWI). Over the past few decades, much of the research on elastic FWI (Lailly, 1983; Tarantola, 1984; Vigh et al., 2014) has focused on exploiting body waves at the exploration scale. However, surface waves dominate the near-surface wavefield, and their amplitudes are very sensitive to the distribution of the S-wave velocity (V_S). Therefore, it seems more appropriate to use surface waves to characterize near-surface structures.

In the context of near-surface characterization, there are several approaches to obtaining a 2D V_S model by inverting the surface-wave full-waveform data. Tran et al. (2013) develop a 2D time-domain Gauss-Newton Rayleigh-wave FWI to detect possible sinkholes and other anomalies. Groos et al. (2017) propose a complete 2D Rayleigh-wave FWI workflow to reconstruct shallow small-scale lateral changes in the V_S structure. Dokter et al. (2017) and Köhn et al. (2019) apply SH-FWI (where SH stands for S-wave polarized in the horizontal direction) for mapping the near-surface small-scale structures at archaeological sites.

To date, most of these field applications of FWI have been demonstrated on near-surface seismic data along 2D lines. Next to the desired events, the recorded data might additionally contain relatively stronger seismic noise and suffer from interference due to 3D scattering from crossline objects. In 2D elastic FWI, the algorithm will try to mimic these additional events associated with wave propagation, which may cause strong artificial heterogeneity in the resulting 2D models. To mitigate these pitfalls, these additional events should be suppressed before the application of FWI, whereas the surface-wave response from the structures below the investigated 2D seismic survey line should be preserved.

In this study, we propose to retrieve the dominant surface-wave responses along the inline direction in a data-driven manner using supervirtual interferometry (SVI) (Bharadwaj et al., 2011; Dai et al., 2011; Place et al., 2019; Liu et al., 2021). We correct the amplitude and phase errors from the retrieval procedure by means of SVI using matched filters (Fomel, 2007). We then invert the resulting surface-wave waveforms in the time domain to estimate the near-surface V_S structure. After a short description of each step, we will apply our proposed FWI workflow to seismic data acquired over an archaeological site.

Manuscript received by the Editor 14 September 2021; revised manuscript received 13 August 2022; published ahead of production 4 September 2022; published online 25 October 2022.
[1]Delft University of Technology, Faculty of Civil Engineering and Geosciences, Delft, The Netherlands. E-mail: j.liu-4@outlook.com (corresponding author); d.s.draganov@tudelft.nl; r.ghose@tudelft.nl.

METHODOLOGY

During the acquisition of a 2D near-surface seismic data set, events reflected (or scattered) from crossline objects also are recorded in the shot gathers. In 2D FWI, the algorithm tries to mimic these events, and hence, artificial subsurface objects are produced. To reduce such incoherent noise or 3D events, we make use of SVI to retrieve and enhance the inline surface waves. We then apply a matched filter to correct for the amplitude and phase errors that unavoidably occur during the procedure of SVI. The resulting data then can be input to the 2D FWI algorithm for subsurface imaging. The complete workflow consisting of all these steps is summarized in Figure 1. Our workflow is designed for surface waves (e.g., Rayleigh waves and Love waves). In this paper, we focus on inverting SH-wave field data. For Rayleigh waves, the propagation depends not only on the subsurface distribution of V_S and density (ρ) but also on the P-wave velocity (V_P). In contrast, the propagation of Love waves requires only knowledge of V_S and ρ. Compared with PSV-FWI (where P stands for the P waves and SV stands for the S waves polarized in the vertical direction when propagating horizontally), SH-FWI requires less computational resources due to the reduced size of the parameter space (Dokter et al., 2017). In addition, SH-FWI performs better on mitigating possible trade-offs between different parameter classes. In the following, we will present the theory behind each step in detail.

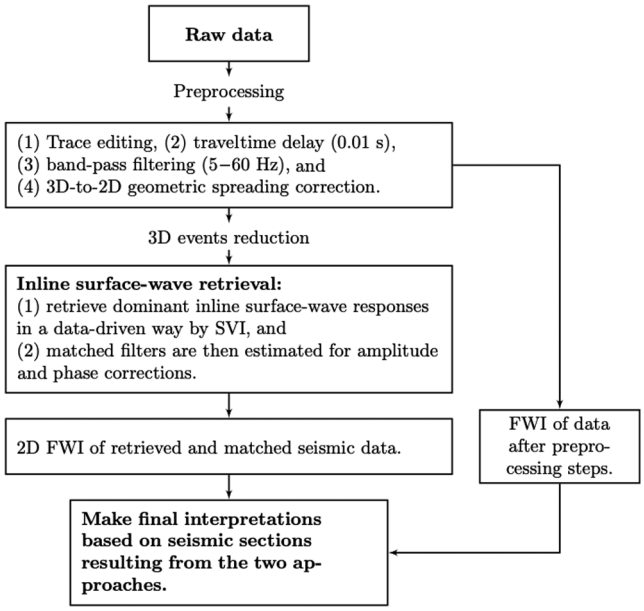

Figure 1. The main workflow proposed in this paper. Note that the preprocessing steps will differ per data set.

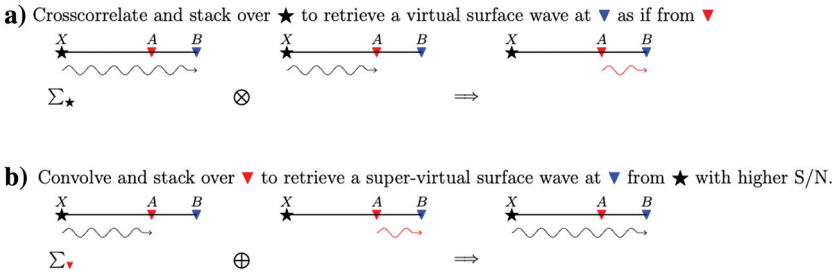

Figure 2. The step for retrieving dominant shot-to-receiver surface waves between source X and receiver B by SVI. The symbols ⊗ and ⊕ denote the crosscorrelation- and crossconvolution-based operators, respectively; ⇝ represents the surface waves propagating along the earth's surface; and the symbols ★ and ▼ represent the active source and receiver, respectively.

Inline surface-wave retrieval by SVI

SVI has been first proposed to enhance the refraction signals at far offsets (Bharadwaj et al., 2011; Place et al., 2019) and later modified to enhance weak diffraction signals (Dai et al., 2011; Liu et al., 2021). The procedure for retrieving and enhancing the shot-to-receiver surface waves is similar, and it is shown in Figure 2. In Figure 2a, ⇝ indicates the surface waves propagating from an active source X to receivers along the earth's surface. The surface waves recorded at receivers A and B can be denoted as $u(X_A, X_i)$ and $u(X_B, X_i)$, respectively. By crosscorrelating these two recordings, we can obtain the virtual surface wave (red ⇝) at B as if it were coming from a virtual source at A. The traveltime of these virtual waves is the same as at other actual source positions as long as they fall inside the stationary-phase region (Snieder, 2004), so they can be stacked constructively to retrieve the surface waves propagating from A to B. In the frequency domain, this step can be formulated as (Wapenaar and Fokkema, 2006; Halliday et al., 2007)

$$C_{X_B X_A} = \sum_{i=1}^{N} u^*(X_A, X_i) \cdot u(X_B, X_i), \tag{1}$$

where $C_{X_B X_A}$ denotes the retrieved receiver-to-receiver surface waves propagating from A to B. The superscript $*$ denotes the complex conjugation in the frequency domain, which corresponds to the time-reversal operation in the time domain and N represents the number of sources available for stacking.

To further obtain shot-to-receiver surface waves propagating from X to B, additional convolution and stacking steps follow. This is demonstrated in Figure 2b, in which the retrieved virtual surface wave (red ⇝) is convolved with an actually recorded surface-wave arrival at a receiver position A from the source at X to produce a supervirtual wave at B. For all receiver positions A located between the source X and the receiver at B, the supervirtual wave is kinematically equivalent. Thus, the retrieved surface waves can be further enhanced by stacking supervirtual surface waves over different receiver positions A, which can be expressed in the frequency domain as

$$C_{X_B X_i} = \sum_{X_A} C_{X_B X_A} \cdot u(X_A, X_i), \tag{2}$$

where $C_{X_B X_i}$ denotes the retrieved shot-to-receiver surface waves. Contrary to traditional seismic interferometry (SI) for surface-wave retrieval and suppression (Konstantaki et al., 2015; Liu et al., 2018; Balestrini et al., 2019), this SVI approach relaxes the requirement that an active shot and a receiver should coexist at the same position for adaptive subtraction.

Matched filter estimation

To accurately retrieve the amplitude of the seismic response using equations 1 and 2, there are several requirements to be fulfilled according to the theory of SI (Draganov et al., 2006; Wapenaar and Fokkema, 2006): the sources should illuminate the receivers homogeneously, the enclosing source boundary should be a sphere with a large radius, the medium at and outside the source boundary should be homogeneous, and the medium parameters should change smoothly across the source boundary. In addition, the application of equation 1 assumes a lossless medium. Note also, that for the retrieval of higher-mode surface waves, sources are required also in the shallow (in the wavelength sense) subsurface (Kimman and Trampert, 2010; van Dalen et al., 2013). These requirements are very difficult to be met in conventional 2D near-surface seismic surveys, where the active sources and receivers are normally deployed only at the surface. Thus, the retrieved surface waves will be characterized by amplitude errors and possibly even phase errors.

To make the retrieved surface waves suitable for FWI, these errors should be corrected. We estimate a nonstationary matched filter (Fomel, 2007, 2009) to account for these errors, by solving the following least-squares inversion problem:

$$\min |\sum_{\gamma} C_{X_B X_i}(\gamma t) * \mathbf{f}(\gamma, t) - D_{X_B X_i}(t)|^2, \tag{3}$$

where $C_{X_B X_i}$ and $D_{X_B X_i}$ are, respectively, the retrieved and recorded surface waves at receiver X_B from the source position X_i; $*$ is the convolution operator; $\mathbf{f}(\gamma, t)$ is the estimated nonstationary matched filter; and γ is a stretching variable. Equation 3 presents an ill-posed problem because it contains more unknown variables than constraints. One remedy is to add additional constraints, i.e., perform regularization, to limit the variability of the filter coefficient $\mathbf{f}(\gamma, t)$. With shaping regularization (Fomel, 2007), equation 3 can be solved as

$$\mathbf{f}(\gamma, t) = \frac{\mathbf{S}\mathbf{P}^T\mathbf{D}}{[\lambda^2\mathbf{I} + \mathbf{S}(\mathbf{P}^T\mathbf{P} - \lambda^2\mathbf{I})]^{-1}}, \tag{4}$$

where λ is a scaling coefficient, defined as $\lambda = |C_{X_B X_i}(t)|^2$. The terms $\mathbf{P}$ and $\mathbf{D}$ are the diagonal matrices composed of $C_{X_B X_i}(\gamma t)$ and $D_{X_B X_i}$, respectively. The term $\mathbf{I}$ is the identity operator in the data space and $\mathbf{S}$ represents the shaping operator which, for this application, we have chosen to be a triangular smoothing operator. In the procedure of shaping regularization, the only additional parameter to control is the radius of the smoothing operator. As the smoothing radius increases, the result of the nonstationary matched filter, as regularized by the shaping operator, approaches the result of the stationary matched filter. In practice, we define a triangular smoothing operator with a small radius ($r_1 = 10, r_2 = 5$), which can significantly suppress the incoherent noise and 3D scattering events, while preserving the inline surface waves. After estimating the filter coefficients through equation 4, we convolve them with the retrieved surface waves ($\sum_{\gamma} C_{X_B X_i}(\gamma t) * \mathbf{f}(\gamma, t)$) to account for the errors. The resulting data will be dominated by inline surface waves, whereas incoherent noise and other 3D events from the crossline direction will be suppressed. Thus, these data are suitable for 2D elastic FWI to characterize 2D subsurface structures.

Theory of 2D SH-FWI

FWI (Lailly, 1983; Tarantola, 1984) is a method to deduce high-resolution models of the subsurface (such as V_S and ρ) by minimizing the residuals between synthetic and measured data. The method consists of two main steps. One is to simulate synthetic wavefields by solving the governing wave equation. The second step is to update the model parameters via a nonlinear-inversion approach (such as the conjugate gradient method) until the misfits between the modeled and measured data are negligible.

We use the acquired SH-wave data. Thus, the propagation of waves in a 2D viscoelastic isotropic medium can be described by the following equation (Aki and Richards, 2002; Köhn et al., 2016):

$$\hat{\mathrm{L}}_{kl}(\mathbf{x})\mathbf{u}_l(\mathbf{x}, t) = f_k(\mathbf{x}, t), \tag{5}$$

where $\mathbf{u}_l$ denotes the lth component of the particle-displacement vector, f_k is the directional component of the body force, and $\hat{\mathrm{L}}_{kl}(\mathbf{x})$ is the differential operator:

$$\hat{\mathrm{L}}_{kl}(\mathbf{x}) = \rho(\mathbf{x})\delta_{kl}\frac{\partial^2}{\partial t^2} - \frac{\partial}{\partial x_j}\Psi_{jkml}(\mathbf{x}) * \frac{\partial}{\partial x_m}, \tag{6}$$

where Ψ is the stiffness tensor, which describes the rheology of the medium; δ_{kl} is the Kronecker delta ($\delta_{kl} = 0$ for $k \neq l$; $\delta_{kl} = 1$ for $k = l$); and $*$ denotes the convolutional operator. Equation 5 can be solved by a time-domain 2D finite-difference algorithm (Virieux, 1984). We use convolutional perfectly matched layers absorbing boundary conditions (Komatitsch and Martin, 2007) to damp spurious reflections from the model's left, right, and bottom boundaries. At the model's top boundary, the free-surface condition is implemented by the image technique (Robertsson, 1996) for accurate modeling.

To update the model parameters along the direction where the residuals between the modeled and the measured data decrease, a specific misfit function measuring the difference between computed and measured data should first be defined. Traditionally, a misfit function is defined in a least-squares sense (Tarantola, 1984) to serve the criterion for measuring the similarity between modeled and measured data. However, this kind of misfit function is not very suitable for near-surface seismic field data. This is mainly because the receiver coupling at each source/receiver position is different, resulting in offset-dependent amplitude variations (Dokter et al., 2017). To partly mitigate this problem, we choose to use the amplitude-unbiased misfit function (Bozdağ et al., 2011; Yuan et al., 2020; Liu et al., 2022) to measure the instantaneous-phase coherency between measured and modeled synthetic data. This type of misfit function assigns stronger weights to the phase part of the signals and is explicitly independent of amplitude errors. It is formulated as

$$\begin{aligned} J(\mathbf{m}) &= \frac{1}{4}\sum_{s,r}\int_0^T \{|e^{i\phi_1(t)} - e^{i\phi_2(t)}|^2 - |e^{i\phi_1(t)} + e^{i\phi_2(t)}|^2\}dt \\ &= \frac{1}{4}\sum_{s,r}\int_0^T \left|\frac{d_1(t) + i\mathcal{H}\{d_1(t)\}}{\sqrt{d^2(t) + \mathcal{H}^2\{d_1(t)\}}} - \frac{d_2(t) + i\mathcal{H}\{d_2(t)\}}{\sqrt{s^2(t) + \mathcal{H}^2\{d_2(t)\}}}\right|^2 dt \\ &\quad - \frac{1}{4}\sum_{s,r}\int_0^T \left|\frac{d_1(t) + i\mathcal{H}\{d_1(t)\}}{\sqrt{d^2(t) + \mathcal{H}^2\{d_1(t)\}}} + \frac{d_2(t) + i\mathcal{H}\{d_2(t)\}}{\sqrt{s^2(t) + \mathcal{H}^2\{d_2(t)\}}}\right|^2 dt, \end{aligned} \tag{7}$$

where $J(\mathbf{m})$ is the value of the misfit function; $\mathbf{m}$ denotes the model parameters; $e^{i\phi_1(t)}$ and $e^{i\phi_2(t)}$ are the exponential phases of the measured ($d_1(t)$) and the synthetic data ($d_2(t)$), respectively; $\mathcal{H}\{\cdot\}$ denotes the Hilbert transform; $\sum_{s,r}$ represents the summation over all available sources and receivers; and T is the recording time of the acquired data. To avoid clutter, we omit the dependency of the measured and synthetic data on source position, receiver position, and model $\mathbf{m}$. Using the theory of the complex analysis, equation 7 also can be written as (Fichtner et al., 2008; Bozdağ et al., 2011; Yuan et al., 2020; Liu et al., 2022; Tohti et al., 2022)

$$J(\mathbf{m}) = \frac{1}{2}\sum_{s,r}\int_0^T \left\{\sin^2\left(\frac{\phi_1(t)-\phi_2(t)}{2}\right) - \cos^2\left(\frac{\phi_1(t)-\phi_2(t)}{2}\right)\right\} dt, \tag{8}$$

where $\phi_1(t)$ and $\phi_2(t)$ are the instantaneous phases of the measured and synthetic data, respectively. Note from equation 8 that the instantaneous-phase coherency equals one when the two signals have opposite polarity ($\phi_1(t) = -\phi_2(t)$) and equals minus one when the two signals have the same polarity ($\phi_1(t) = \phi_2(t)$). The value of $J(\mathbf{m})$ can be minimized by iteratively updating the model parameters ($\mathbf{m}$), beginning at the initial model ($\mathbf{m}_0$), along a search direction determined by a nonlinear optimization approach, such as the preconditioned conjugate gradient method (Nocedal and Wright, 2006).

Multichannel analysis of surface wave for initial model building

To avoid being trapped in a local minimum, 2D elastic FWI needs a good initial model to start with. In this paper, we use multichannel analysis of surface waves (MASW) to provide the initial V_S model. MASW has been proven to be an efficient means to obtain velocity profiles by inverting the dispersion curves of surface waves (e.g., Xia et al., 1999). Compared to FWI, which uses all the information (amplitude and phase) from a recorded wavefield, MASW uses only the dispersion curve skeletonized from a complex wavefield. Thus, the MASW approach converges more easily; however, the resolution of the extracted structure from MASW will be much lower than that from FWI. Hence, it is beneficial to build the initial models using MASW.

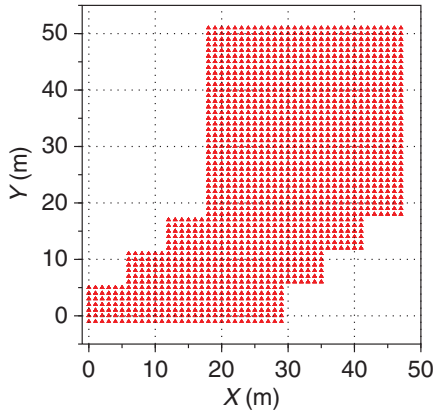

Figure 3. Layout of receiver array used to acquire 2D seismic data in the field using a roll-along approach. The x-axis denotes the lateral positions of receivers, and the y-axis represents the corresponding source positions for each receiver. The triangles represent horizontal, 10 Hz, 1C geophones. Every receiver position at an interval of 1 m is displayed.

MASW includes two steps — the first is to extract the dispersion curve from a recorded shot gather and the second is to fit the picked and the modeled dispersion curves to obtain the velocity models. In this research, we transfer the recorded wavefield data from the time-space (t-x) domain to the frequency-slowness (f-p) domain using the slant-stack approach (McMechan and Yedlin, 1981). The dispersion curves of different modes then can be easily picked. We use the neighborhood algorithm (NA) (Sambridge, 1999; Wathelet, 2008) to minimize the misfit between the picked and computed dispersion curves, resulting in a 1D velocity structure for a specific lateral position.

FIELD DATA EXAMPLE

The study area was located at Dreumel, central Netherlands. The purpose of this survey was to locate/characterize, with high resolution, the presence of ancient boats that were anticipated to be buried under shallow soil cover at this site. We carried out a seismic survey along two lines. We have presented here the FWI results along one of the survey lines.

Field data acquisition

We used a high-frequency S-wave vibrator (Ghose et al., 1996; Ghose, 2012) to excite seismic energy. The receiver array consisted of 120 10-Hz horizontal geophones at an interval of 0.25 m. We oriented the vibrator (source orientation) and the geophones in the crossline direction so that we could generate and record SH waves. We used a roll-along geometry during data acquisition; the layout of the receivers is shown in Figure 3. At each shot position, four recordings were acquired and stacked to yield one common-source gather to enhance the signal-to-noise ratio of the acquired data in the field. In total, 105 common-source gathers were recorded and used subsequently for imaging the subsurface.

Inline surface-wave retrieval

Figure 4a and 4e displays two examples of S-wave common-source gathers after application of crosscorrelation of the raw vibrograms with the estimated groundforce (Ghose, 2002) and followed by two other basic preprocessing steps — trace editing and bandpass filtering between 5 and 60 Hz. We can see that the data are dominated by dispersive Love waves. Underneath those Love waves, we can also identify weak reflection and diffraction events. Although the amplitude of these events (reflections/diffractions) is much lower than those of the Love waves, these events in the recorded data can cause additional problems during the FWI procedure. Especially when inverting the low frequencies, FWI can interpret those reflections/diffractions as part of the Love-wave dispersion, which may lead to artifacts in the 2D inverted models. Therefore, the Love waves should be separated from the other events for further inversion.

Figure 4b and 4f displays the virtual gathers retrieved by SVI (equations 1 and 2 and Figure 2) for a virtual source at the position of the active source in Figure 4a and 4e. Comparing Figure 4a and 4b (and also Figure 4e and 4f), we can see that the main kinematic

characteristics of the Love waves are retrieved well. However, due to the interferometric approximations used in equations 1 and 2, there are errors in the estimated Love waves in Figure 4b and 4f. We correct these errors by estimating a nonstationary matched filter (equation 4) and then convolving this filter with the virtual gather (Figure 4b and 4f), resulting in the matched Love waves (Figure 4c and 4g). The phase and amplitudes of the retrieved Love wave shown in Figure 4c and 4g match well with those in the original active-source shot gather, whereas the weak reflections and diffractions are greatly suppressed (Figure 4d and 4h). In the following, we will mainly make use of shot gathers similar to the one shown in Figure 4c for the FWI procedure.

FWI results

The recorded wavefields are excited by a spatially limited (point) source, whereas the 2D elastic FWI considers 2D wave propagation modeled with a line source. To compensate for this, we turn the recorded seismic wavefield into its equivalent line-source wavefield by the single-velocity transformation approach (Forbriger et al., 2014; Schäfer et al., 2014). To stabilize the procedure of source-wavelet estimation using a Wiener-deconvolution approach (Groos et al., 2017), we delay the whole common-source gather by 0.01 s. We also kill the traces falling inside the near-offset range (less than 1 m) because such near-offset traces are partly clipped and thus contain less information about the subsurface (Pan et al., 2019). Noise before the first arrivals is muted. In addition, we normalize each trace by its maximum to eliminate the amplitude uncertainties and thus improve the inversion results (Louboutin et al., 2017). These preprocessing steps are applied to common-source gathers (Figure 4a and 4c), which are subsequently used in FWI.

To avoid being trapped in local minima, proper initial models are required. We estimate the initial model through the MASW approach described earlier. Figure 5a shows a shot gather of the retrieved Love waves after SVI and matched filtering for a source located at 18.5 m. The corresponding dispersion image of the retrieved wavefield is shown in Figure 5b. We pick the dispersion curve (the dashed white line in Figure 5b) along with the maximum energy in the dispersion image. We generate 30,000 models using the NA approach and select the best model whose theoretical dispersion curve fits best the picked one. The computed dispersion curve (the black curve in Figure 5b) from the best V_S model (the black line in Figure 5c) is plotted together with the picked dispersion data. Because the dispersion images calculated at other lateral positions are similar, we use only the inverted V_S structure at this position to build the laterally homogeneous V_S model, by extending the 1D model in the horizontal direction. The initial V_S model is shown in Figure 5d. We discretize the model with 215×40 grid points in the x- and z-directions, with a grid spacing of 0.25 m. To ensure the stability of wave simulation, we choose a timestep of 50 ms with a recording time of 0.2 s. The density model is assumed to be known and kept constant at $1800\,\mathrm{kg/m^3}$. We choose a constant quality factor ($Q_S = 20$) (Bohlen, 2002; Cheng et al., 2018) to account for the strong attenuation effects at the near surface. We have determined this optimal Q-value by repeating the inversion for a set of constant quality factors and using the relative objective function (Figure 6) to select the optimum Q-value.

Starting from this initial model, we apply elastic FWI by first inverting a subset of the data within the frequency band of 5–10 Hz. The upper corner frequency of the passband is subsequently increased to 20, 30, 40, and 50 Hz. The FWI result from each frequency band is used as the initial model for the next frequency band. We move to the next frequency band once the improvement in the misfit value for the current frequency band becomes smaller than 1%

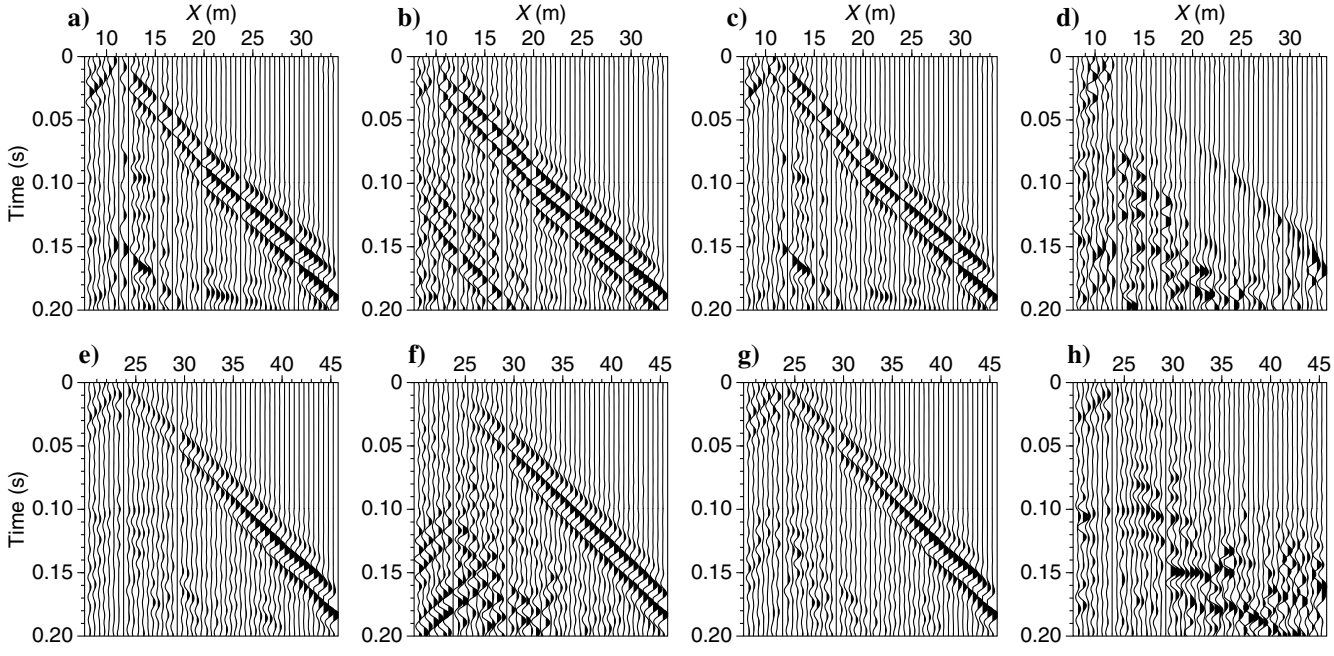

Figure 4. (a) A typical preprocessed SH-wave shot gather. The preprocessing steps include trace editing and band-pass filtering (5–60 Hz): (b) retrieved supervirtual Love waves for a virtual source located at a position as shown in (a), (c) result after convolution of the data in (b) with a nonstationary matched filter to account for the errors in the retrieval during the procedure of SVI, and (d) result after subtraction of (c) from (a). (e–h) As shown in (a–d) but for a common-source gather with a different source position. Every second trace is plotted.

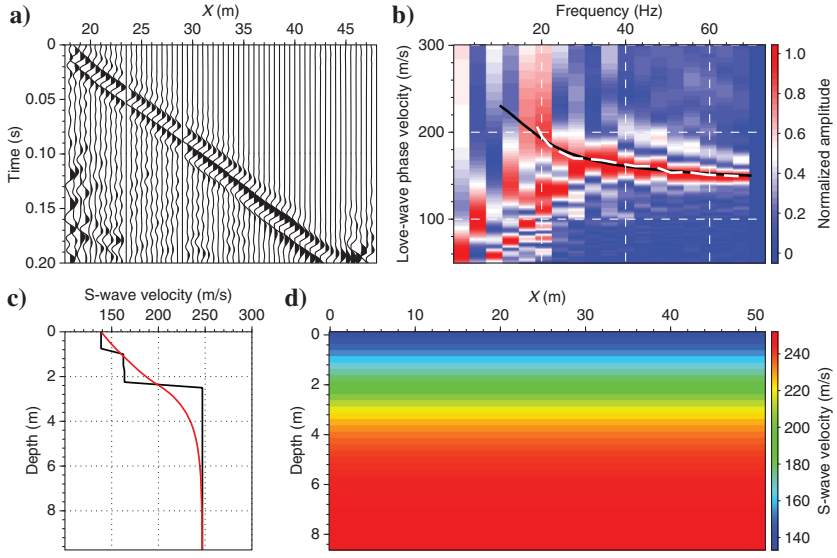

Figure 5. (a) An example field shot gather showing retrieved Love waves after SVI and matched filtering, as shown in Figure 4c, for a source located at 18.5 m. Every second trace is plotted. (b) Dispersion image of the data in (a) calculated by a slant-stack procedure. The dashed white line denotes the picked Love-wave dispersion curve of the fundamental mode. The black line is the theoretical dispersion curve calculated from the finally inverted V_S profile as shown in (c). (c) Estimated 1D V_S structure (the black line) obtained by minimizing the misfit between picked and computed dispersion curves. Such minimization is performed with the NA using the code from Wathelet et al. (2020). The red line represents the smoothed version of the estimated structure (the black line), which is then extended laterally to build the initial, laterally homogeneous V_S model, as shown in (d), for the subsequent elastic FWI.

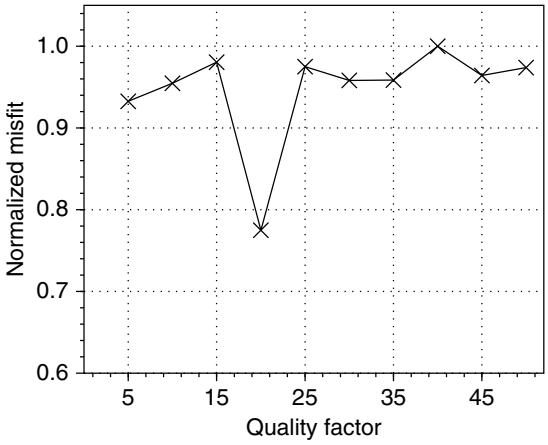

Figure 6. Determination of the optimum quality factor by repeating the inversion for a set of constant Q values. The least-squares misfit between the synthetic and measured data for each inversion is displayed.

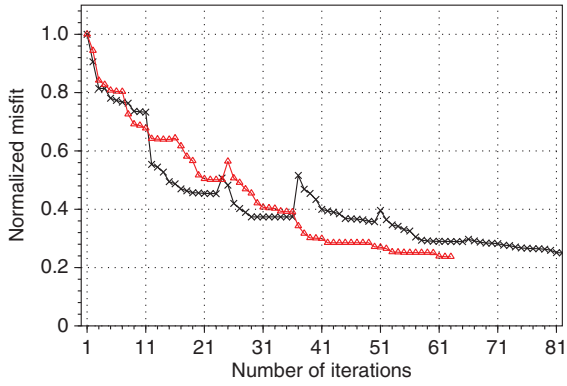

Figure 7. Evolution of the normalized misfit values during FWI of data illustrated in Figure 4a (the black line) and FWI of data illustrated in Figure 4c (the red line). Note that FWI of data after the procedure of SVI and matched filter converges faster.

Figure 8. (a) The V_S model obtained by FWI applied to data shown in Figure 4c. (b) Comparison between the 1D inverted V_S profile from FWI (red line) and the 1D initial V_S profile from MASW (black line) at x = 10 m, and (c–e) the same as (b) but at x = 20, 30, and 40 m, respectively. These lateral positions are indicated by the dashed white lines in (a).

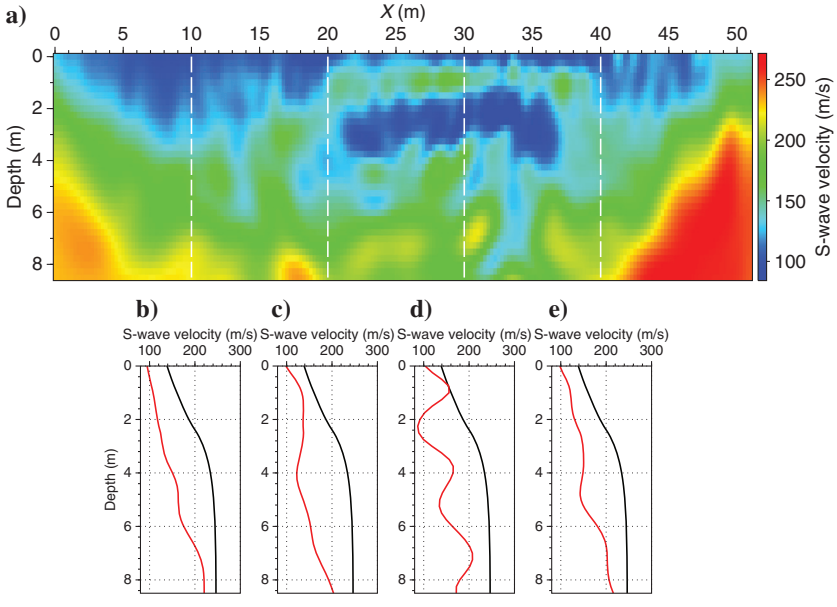

between two consecutive iterations. This also serves as the abort criterion for the last stage in which a subset of the data within the frequency band of 5–50 Hz is inverted. To obtain an update at the shallower part, we precondition the gradients using a semicircular taper (Groos et al., 2017) with a length of 3 m. We also smooth the gradients and models by a 2D Gaussian filter (Ravaut et al., 2004) with a length of approximately half of the dominant wavelength. This is done to avoid the occurrence of small-scale artifacts below the FWI resolution limit and make the inversion stable. The evolution of the normalized least-squares misfit functions during FWI of the field data is shown in Figure 7, in which the normalized misfit reduces from 1.0 at the first iteration to approximately 0.2 at the final iteration.

The FWI of the dominant Love waves retrieved by SVI and matched filtering converges after a total of 63 iterations. Figure 8a shows the final inverted V_S results for the frequency band of 5–50 Hz. To show how FWI has improved the subsurface V_S structures, we have plotted slices of the 1D inverted V_S profile from FWI (Figure 8a) and the 1D initial V_S profile from MASW (Figure 5d) at x = 10, 20, 30, and 40 m, respectively. Based on the final inverted V_S model, we model the synthetic data using source wavelets as shown in Figure 9. These source wavelets are estimated by a stabilized Wiener-deconvolution approach (Groos et al., 2017). In Figure 10a and 10c, we show the overlay for two source positions

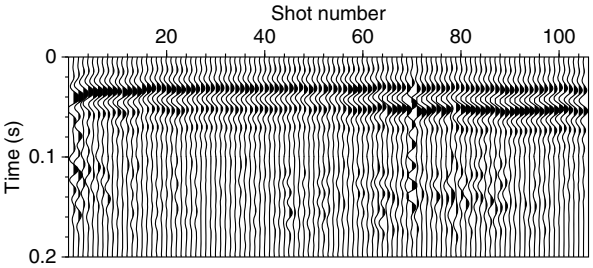

Figure 9. Estimated source wavelets for the 105 shot gathers (Figure 4c) with a frequency band between 5 and 50 Hz.

of the shot gathers with the Love waves retrieved by SVI and matched filtering, and the shot gathers with the synthetic Love waves and also their residuals. From the overlay of these two gathers, we can see that

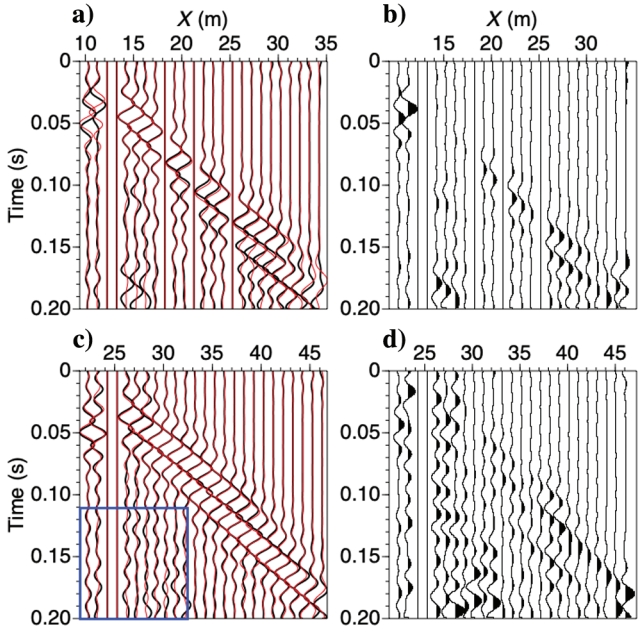

Figure 10. (a) The overlay between the measured data as shown in Figure 4c (the black lines) and synthetic data (the red lines) generated using the inverted V_S model from Figure 8a and using the source signatures from Figure 9. (b) The residuals between the measured and synthetic data in (a). (c and d) The same as shown above (a and b) but for a source at a different lateral location. Data are band-limited within the frequency range 5–50 Hz. The blue rectangle highlights the area where weak events (reflections/diffractions) in the measured data have been efficiently suppressed by the combination of SVI and nonstationary matched filter; a significantly better waveform fitting is observed compared with the same area indicated in Figure 12. Traces are normalized using the maximum value. For visualization purposes, every fourth trace is plotted here.

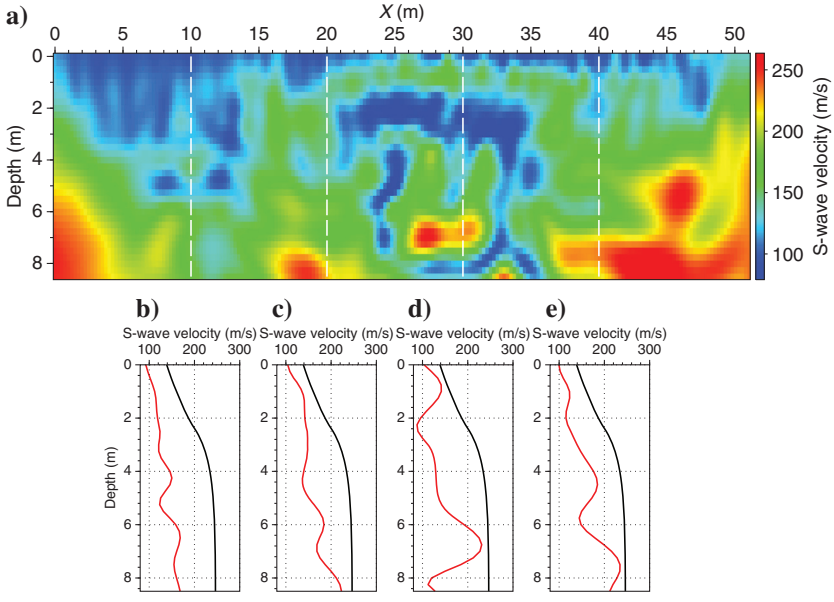

Figure 11. (a) The V_S model obtained by FWI applied to data as shown in Figure 4a. (b) Comparison between the 1D inverted V_S profile from FWI (the red line) and the 1D initial V_S profile from MASW (the black line) at x = 10 m and (c–e) the same as (b) but at x = 20, 30, and 40 m, respectively. These lateral positions are indicated by the dashed white lines in (a).

the main events across the entire offset range match quite well without any obvious cycle skipping. The residuals (Figure 10b and 10d) are small across the entire source-receiver offset range, except for receivers located far away from the source locations.

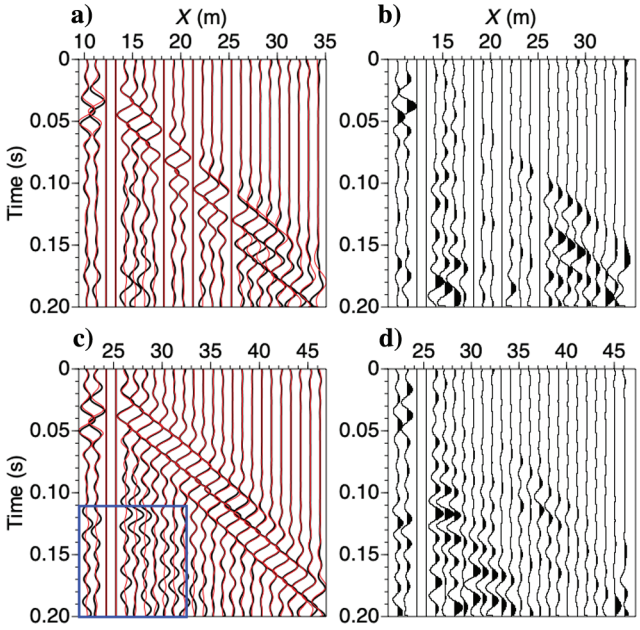

Figure 12. The same as Figure 10, but for measured data as in Figure 4a. The blue rectangle in (c) highlights the area where weak events (reflections/diffractions) in the measured data have not been suppressed, thus a significantly worse waveform fitting is observed compared to the same area indicated in Figure 10.

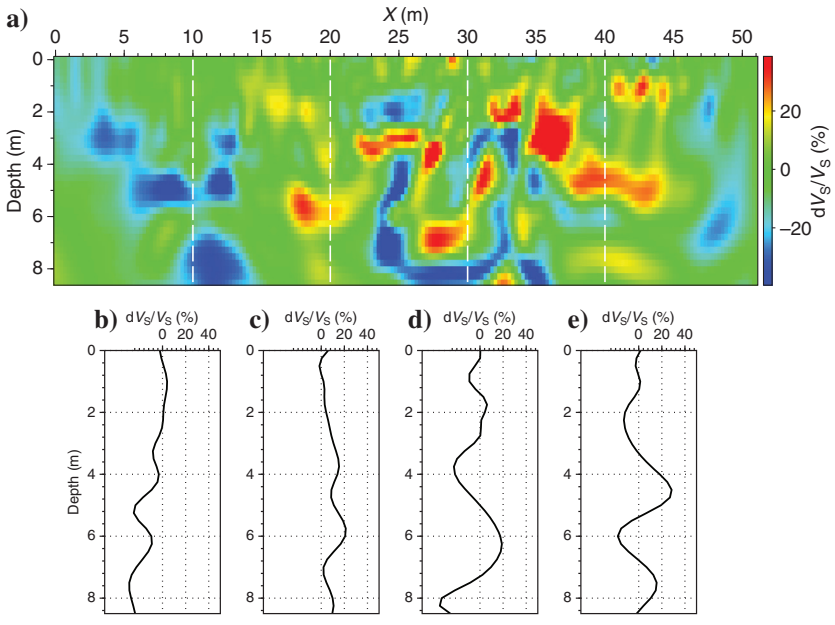

Figure 13. (a) The V_S uncertainties calculated by $(V_1 - V_2)/V_1$, where V_1 denotes the inverted V_S model from Figure 8a and V_2 denotes the inverted V_S model from Figure 11a. (b) Slice of 1D-estimated V_S uncertainties at x = 10 m from (a), and (c–e) the same as (b) but for x = 20, 30, and 40 m, respectively.

For a comparison, we also run FWI on the preprocessed data as shown in Figure 4a, i.e., without suppression of incoherent noise and 3D scattering events. The inverted V_S models for the final frequency band of 5–50 Hz are shown in Figure 11. In Figure 11, we also plot slices of the 1D inverted V_S profile from FWI and the 1D initial V_S profile from MASW at different lateral locations. The overlay between the measured wavefield (Figure 4a), synthetic data associated with the final inverted V_S model, and their residuals are shown in Figure 12, whose source positions are the same as the source positions for the shot gathers shown in Figure 10. As we can see from Figure 12a and 12c, the dominant events (mainly Love waves) over all available source-receiver offset ranges match well, without the cycle-skipping problem. However, the weak events in the observed gathers cannot be simulated in the synthetic data (the blue rectangle in Figure 12d). Because these events have been suppressed well in the data as shown in Figure 10a and 10c by a combination of SVI and nonstationary matched filtering, we can see a significantly improved waveform fitting in the same area (the blue rectangle in Figure 10d).

The final inversion result of FWI of the dominant Love waves retrieved by SVI and matched filtering is shown in Figure 8a. At lateral location 5–20 m, a low-velocity area (100–120 m/s) is located at a shallow depth (0–2.5 m). Another low-velocity area also can be identified at the lateral position 20–37 m, which extends to a greater depth (1–4 m). The final 2D V_S profile obtained from the FWI of the preprocessed field data without the suppression of incoherent noise and the 3D scattering events is shown in Figure 11a, in which two low-velocity anomalies are imaged at similar positions as shown in Figure 8a. Figure 13a shows the V_S uncertainties calculated by $(V_1 - V_2)/V_1$, where V_1 denotes the inverted V_S model from Figure 8a and V_2 denotes the inverted V_S structure from Figure 11a. Areas with low uncertainties can be interpreted with more confidence. For the two low-velocity areas identified in Figures 8a and 11a, the corresponding V_S uncertainties are low (see Figure 13b and 13d). This means that these low-velocity areas are constrained well. Because we do not have any other subsurface information about this area, the final interpretation of these low-velocity areas has to be corroborated by other independent archaeological investigations.

CONCLUSION

We proposed a complete 2D elastic FWI workflow for the inversion of near-surface propagating Love waves. To mitigate the artifacts caused by seismic noise and the 3D events scattered from objects in the crossline direction, we proposed to make use of a combination of SVI and matched filtering to accurately retrieve the dominant inline surface waves (Love waves). Compared with the computational costs of performing FWI, the computational costs for retrieving the dominant inline surface waves through our approach were negligible. We then applied 2D elastic SH-FWI to the retrieved Love-wave waveforms to deduce a high-resolution S-wave velocity model of the subsurface structure. The results showed that our workflow is stable; the results can be interpreted together with the model inferred from the inver-

sion of the original data to mitigate the potential misinterpretation of artifacts caused by 3D effects.

ACKNOWLEDGMENTS

The first author would like to thank the financial support from the China Scholarship Council (file no. 201604910851). The field data were acquired with the assistance of D. Ngan-Tillard, J. Brackenhoff, and J. van den Berg.

DATA AND MATERIALS AVAILABILITY

Data associated with this research are available and can be obtained by contacting the corresponding author.

REFERENCES

Aki, K., and P. G. Richards, 2002, Quantitative seismology: University Science Books.

Balestrini, F., D. Draganov, A. Malehmir, P. Marsden, and R. Ghose, 2019, Improved target illumination at Ludvika mines of Sweden through seismic-interferometric surface-wave suppression: Geophysical Prospecting, **68**, 200–213, doi: 10.1111/1365-2478.12890.

Bharadwaj, P., G. Schuster, I. Mallinson, and W. Dai, 2011, Theory of supervirtual refraction interferometry: Geophysical Journal International, **188**, 263–273, doi: 10.1111/j.1365-246X.2011.05253.x.

Bohlen, T., 2002, Parallel 3-D viscoelastic finite difference seismic modelling: Computers & Geosciences, **28**, 887–899, doi: 10.1016/S0098-3004(02)00006-7.

Bozdağ, E., J. Trampert, and J. Tromp, 2011, Misfit functions for full waveform inversion based on instantaneous phase and envelope measurements: Geophysical Journal International, **185**, 845–870, doi: 10.1111/j.1365-246X.2011.04970.x.

Cheng, F., D. Draganov, J. Xia, Y. Hu, and J. Liu, 2018, Q-estimation using seismic interferometry from vertical well data: Journal of Applied Geophysics, **159**, 16–22, doi: 10.1016/j.jappgeo.2018.07.019.

Dai, W., T. Fei, Y. Luo, and G. T. Schuster, 2011, Super-virtual interferometric diffractions as guide stars: 81st Annual International Meeting, SEG, Expanded Abstracts, 3819–3823, doi: 10.1190/1.3628002.

Dokter, E., D. Köhn, D. Wilken, D. D. Nil, and W. Rabbel, 2017, Full waveform inversion of SH- and Love-wave data in near-surface prospecting: Geophysical Prospecting, **65**, 216–236, doi: 10.1111/1365-2478.12549.

Draganov, D., K. Wapenaar, and J. Thorbecke, 2006, Seismic interferometry: Reconstructing the earth's reflection response: Geophysics, **71**, no. 4, SI61–SI70, doi: 10.1190/1.2209947.

Fichtner, A., B. L. N. Kennett, H. Igel, and H.-P. Bunge, 2008, Theoretical background for continental- and global-scale full-waveform inversion in the time-frequency domain: Geophysical Journal International, **175**, 665–685, doi: 10.1111/j.1365-246X.2008.03923.x.

Fomel, S., 2007, Shaping regularization in geophysical-estimation problems: Geophysics, **72**, no. 2, R29–R36, doi: 10.1190/1.2433716.

Fomel, S., 2009, Adaptive multiple subtraction using regularized nonstationary regression: Geophysics, **74**, no. 1, V25–V33, doi: 10.1190/1.3043447.

Forbriger, T., L. Groos, and M. Schäfer, 2014, Line-source simulation for shallow-seismic data. Part 1: Theoretical background: Geophysical Journal International, **198**, 1387–1404, doi: 10.1093/gji/ggu199.

Ghose, R., 2002, High-frequency shear wave reflections from shallow subsoil layers using a vibrator source: Sweep cross-correlation versus deconvolution with groundforce derivative: 72nd Annual International Meeting, SEG, Expanded Abstracts, 1408–1411, doi: 10.1190/1.1816924.

Ghose, R., 2012, A microelectromechanical system digital 3C array seismic cone penetrometer: Geophysics, **77**, no. 3, WA99–WA107, doi: 10.1190/geo2011-0266.1.

Ghose, R., J. Brouwer, and V. Nijhof, 1996, A portable S-wave vibrator for high-resolution imaging of the shallow subsurface: 58th Annual International Conference and Exhibition, EAGE, Extended Abstracts, cp-48-00132, doi: 10.3997/2214-4609.201408721.

Groos, L., M. Schäfer, T. Forbriger, and T. Bohlen, 2017, Application of a complete workflow for 2D elastic full-waveform inversion to recorded shallow-seismic Rayleigh waves: Geophysics, **82**, no. 2, R109–R117, doi: 10.1190/geo2016-0284.1.

Halliday, D. F., A. Curtis, J. O. A. Robertsson, and D.-J. van Manen, 2007, Interferometric surface-wave isolation and removal: Geophysics, **72**, no. 5, A69–A73, doi: 10.1190/1.2761967.

Kimman, W. P., and J. Trampert, 2010, Approximations in seismic interferometry and their effects on surface waves: Geophysical Journal International, **182**, 461–476, doi: 10.1111/j.1365-246X.2010.04632.x.

Köhn, D., T. Meier, M. Fehr, D. D. Nil, and M. Auras, 2016, Application of 2D elastic Rayleigh waveform inversion to ultrasonic laboratory and field data: Near Surface Geophysics, **14**, 461–467, doi: 10.3997/1873-0604.2016027.

Köhn, D., D. Wilken, D. D. Nil, T. Wunderlich, W. Rabbel, L. Werther, J. Schmidt, C. Zielhofer, and S. Linzen, 2019, Comparison of time-domain SH waveform inversion strategies based on sequential low and bandpass filtered data for improved resolution in near-surface prospecting: Journal of Applied Geophysics, **160**, 69–83, doi: 10.1016/j.jappgeo.2018.11.001.

Komatitsch, D., and R. Martin, 2007, An unsplit convolutional perfectly matched layer improved at grazing incidence for the seismic wave equation: Geophysics, **72**, no. 5, SM155–SM167, doi: 10.1190/1.2757586.

Konstantaki, L., D. Draganov, R. Ghose, and T. Heimovaara, 2015, Seismic interferometry as a tool for improved imaging of the heterogeneities in the body of a landfill: Journal of Applied Geophysics, **122**, 28–39, doi: 10.1016/j.jappgeo.2015.08.008.

Lailly, P., 1983, The seismic inverse problem as a sequence of before stack migrations, *in* J. B. Bednar, E. Robinson, and A. Weglein, eds., Conference on Inverse Scattering — Theory and Application: SIAM, 206–220.

Lambot, S., E. Slob, D. Chavarro, M. Lubczynski, and H. Vereecken, 2008, Measuring soil surface water content in irrigated areas of southern Tunisia using full-waveform inversion of proximal GPR data: Near Surface Geophysics, **6**, 403–410, doi: 10.3997/1873-0604.2008028.

Liu, J., D. Draganov, and R. Ghose, 2018, Seismic interferometry facilitating the imaging of shallow shear-wave reflections hidden beneath surface waves: Near Surface Geophysics, **16**, 372–382, doi: 10.3997/1873-0604.2018013.

Liu, J., D. Draganov, R. Ghose, and Q. Bourgeois, 2021, Near-surface diffractor detection at archaeological sites based on an interferometric workflow: Geophysics, **86**, no. 3, WA1–WA11, doi: 10.1190/geo2020-0142.1.

Liu, J., R. Ghose, and D. Draganov, 2022, Characterizing near-surface structures at the Ostia archaeological site based on instantaneous-phase coherency inversion: Geophysics, **87**, no. 4, R337–R348, doi: 10.1190/geo2021-0467.1.

Louboutin, M., L. Guasch, and F. Herrmann, 2017, Data normalization strategies for full-waveform inversion: 79th Annual International Conference and Exhibition, EAGE, Extended Abstracts, doi: 10.3997/2214-4609.201700720.

McMechan, G. A., and M. J. Yedlin, 1981, Analysis of dispersive waves by wave field transformation: Geophysics, **46**, 869–874, doi: 10.1190/1.1441225.

Mecking, R., D. Köhn, M. Meinecke, and W. Rabbel, 2021, Cavity detection by SH-wave full-waveform inversion — A reflection-focused approach: Geophysics, **86**, no. 3, WA123–WA137, doi: 10.1190/geo2020-0349.1.

Nguyen, T. D., and K. T. Tran, 2018, Site characterization with 3D elastic full-waveform tomography: Geophysics, **83**, no. 5, R389–R400, doi: 10.1190/geo2017-0571.1.

Nocedal, J., and S. Wright, 2006, Numerical optimization: Springer Science & Business Media.

Pan, Y., L. Gao, and T. Bohlen, 2019, High-resolution characterization of near-surface structures by surface-wave inversions: From dispersion curve to full waveform: Surveys in Geophysics, **40**, 167–195, doi: 10.1007/s10712-019-09508-0.

Place, J., D. Draganov, A. Malehmir, C. Juhlin, and C. Wijns, 2019, Cross-coherence-based interferometry for the retrieval of first arrivals and subsequent tomographic imaging of differential weathering: Geophysics, **84**, no. 4, Q37–Q48, doi: 10.1190/geo2018-0405.1.

Ravaut, C., S. Operto, L. Improta, J. Virieux, A. Herrero, and P. Dell'Aversana, 2004, Multiscale imaging of complex structures from multifold wide-aperture seismic data by frequency-domain full-waveform tomography: Application to a thrust belt: Geophysical Journal International, **159**, 1032–1056, doi: 10.1111/j.1365-246X.2004.02442.x.

Robertsson, J. O. A., 1996, A numerical free-surface condition for elastic/viscoelastic finite-difference modeling in the presence of topography: Geophysics, **61**, 1921–1934, doi: 10.1190/1.1444107.

Sambridge, M., 1999, Geophysical inversion with a neighbourhood algorithm — I. Searching a parameter space: Geophysical Journal International, **138**, 479–494, doi: 10.1046/j.1365-246X.1999.00876.x.

Schäfer, M., L. Groos, T. Forbriger, and T. Bohlen, 2014, Line-source simulation for shallow-seismic data. Part 2: Full-waveform inversion — A synthetic 2-D case study: Geophysical Journal International, **198**, 1405–1418, doi: 10.1093/gji/ggu171.

Snieder, R., 2004, Extracting the Green's function from the correlation of coda waves: A derivation based on stationary phase: Physical Review E, **69**, 046610, doi: 10.1103/PhysRevE.69.046610.

Tarantola, A., 1984, Inversion of seismic reflection data in the acoustic approximation: Geophysics, **49**, 1259–1266, doi: 10.1190/1.1441754.

Tohti, M., J. Liu, W. Xiao, Y. Wang, Q. Di, and K. Zhou, 2022, Full-waveform inversion of surface waves based on instantaneous-phase coherency: Near Surface Geophysics, **20**, 494–506, doi: 10.1002/nsg.12229.

Tran, K. T., M. McVay, M. Faraone, and D. Horhota, 2013, Sinkhole detection using 2D full seismic waveform tomography: Geophysics, **78**, no. 5, R175–R183, doi: 10.1190/geo2013-0063.1.

van Dalen, K. N., K. Wapenaar, and D. F. Halliday, 2013, Surface wave retrieval in layered media using seismic interferometry by multidimensional deconvolution: Geophysical Journal International, **196**, 230–242, doi: 10.1093/gji/ggt389.

Vigh, D., K. Jiao, D. Watts, and D. Sun, 2014, Elastic full-waveform inversion application using multicomponent measurements of seismic data collection: Geophysics, **79**, no. 2, R63–R77, doi: 10.1190/geo2013-0055.1.

Virieux, J., 1984, SH-wave propagation in heterogeneous media: Velocity-stress finite-difference method: Geophysics, **49**, 1933–1942, doi: 10.1190/1.1441605.

Wapenaar, K., and J. Fokkema, 2006, Green's function representations for seismic interferometry: Geophysics, **71**, no. 4, SI33–SI46, doi: 10.1190/1.2213955.

Wathelet, M., 2008, An improved neighborhood algorithm: Parameter conditions and dynamic scaling: Geophysical Research Letters, **35**, L09301, doi: 10.1029/2008GL033256.

Wathelet, M., J.-L. Chatelain, C. Cornou, G. D. Giulio, B. Guillier, M. Ohrnberger, and A. Savvaidis, 2020, Geopsy: A user-friendly open-source tool set for ambient vibration processing: Seismological Research Letters, **91**, 1878–1889, doi: 10.1785/0220190360.

Xia, J., R. D. Miller, and C. B. Park, 1999, Estimation of near-surface shear-wave velocity by inversion of Rayleigh waves: Geophysics, **64**, 691–700, doi: 10.1190/1.1444578.

Yuan, Y. O., E. Bozdağ, C. Ciardelli, F. Gao, and F. J. Simons, 2020, The exponentiated phase measurement, and objective-function hybridization for adjoint waveform tomography: Geophysical Journal International, **221**, 1145–1164, doi: 10.1093/gji/ggaa063.

Biographies and photographs of the authors are not available.